

7-12-2017

Chemical Disorder in Topological Insulators: A Route to Magnetism Tolerant Topological Surface States

M. Carmen Martínez-Velarte
University of Zaragoza

Bernhard Kretz
Donostia International Physics Center

María Moro-Lagares
University of Zaragoza

Myriam H. Aguirre
University of Zaragoza

Trevor A. Riedemann
Follow this and additional works at: https://lib.dr.iastate.edu/mse_pubs
Ames Laboratory, tnr@ameslab.gov

 Part of the [Condensed Matter Physics Commons](#), [Materials Chemistry Commons](#), and the [Materials Science and Engineering Commons](#)
See next page for additional authors

The complete bibliographic information for this item can be found at https://lib.dr.iastate.edu/mse_pubs/304. For information on how to cite this item, please visit <http://lib.dr.iastate.edu/howtocite.html>.

Chemical Disorder in Topological Insulators: A Route to Magnetism Tolerant Topological Surface States

Abstract

We show that the chemical inhomogeneity in ternary three-dimensional topological insulators preserves the topological spin texture of their surface states against a net surface magnetization. The spin texture is that of a Dirac cone with helical spin structure in the reciprocal space, which gives rise to spin-polarized and dissipation-less charge currents. Thanks to the nontrivial topology of the bulk electronic structure, this spin texture is robust against most types of surface defects. However, magnetic perturbations break the time-reversal symmetry, enabling magnetic scattering and loss of spin coherence of the charge carriers. This intrinsic incompatibility precludes the design of magnetoelectronic devices based on the coupling between magnetic materials and topological surface states. We demonstrate that the magnetization coming from individual Co atoms deposited on the surface can disrupt the spin coherence of the carriers in the archetypal topological insulator Bi₂Te₃, while in Bi₂Se₂Te the spin texture remains unperturbed. This is concluded from the observation of elastic backscattering events in quasiparticle interference patterns obtained by scanning tunneling spectroscopy. The mechanism responsible for the protection is investigated by energy resolved spectroscopy and ab initio calculations, and it is ascribed to the distorted adsorption geometry of localized magnetic moments due to Se–Te disorder, which suppresses the Co hybridization with the surface states.

Keywords

3D topological insulators, chemical disorder, magnetic atoms, quasiparticle-interference pattern, scanning tunneling microscopy

Disciplines

Condensed Matter Physics | Materials Chemistry | Materials Science and Engineering

Comments

This document is the Accepted Manuscript version of a Published Work that appeared in final form in *Nano Letters*, copyright © American Chemical Society after peer review and technical editing by the publisher. To access the final edited and published work see DOI: [10.1021/acs.nanolett.7b00311](https://doi.org/10.1021/acs.nanolett.7b00311). Posted with permission.

Authors

M. Carmen Martínez-Velarte, Bernhard Kretz, María Moro-Lagares, Myriam H. Aguirre, Trevor A. Riedemann, Thomas A. Lograsso, Luis Morellón, M. Ricardo Ibarra, Arán Garcia-Lekue, and David Serrate

Chemical Disorder in Topological Insulators: A Route to Magnetism Tolerant Topological Surface States

M. Carmen Martínez-Velarte,^{♦,○,§} Bernhard Kretz,^{⊥,¶} María Moro-Lagares,^{♦,○,§} Myriam H. Aguirre,^{♦,○,§} Trevor M. Riedemann,[†] Thomas A. Lograsso,^{‡,‡} Luis Morellón,^{♦,○,§} M. Ricardo Ibarra,^{♦,○,§} Arán García-Lekue,^{⊥,¶} and David Serrate^{*,♦,○,§}

[♦]Instituto de Nanociencia de Aragón (INA) & Laboratorio de Microscopías Avanzadas (LMA), University of Zaragoza, 50018 Zaragoza, Spain

[○]Department of Condensed Matter Physics, University of Zaragoza, 50009 Zaragoza, Spain

[§]Fundación Instituto de Nanociencia de Aragón (FINA), 50018 Zaragoza, Spain

[⊥]Donostia International Physics Center (DIPC), E-20018 San Sebastián, Spain

[†]Ames Laboratory, U.S. Department of Energy, Ames, Iowa 50011, United States

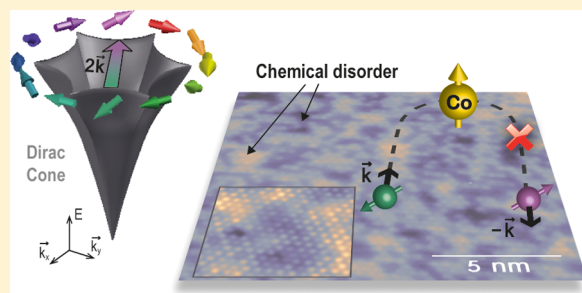
[‡]Department of Materials Sciences & Engineering, Iowa State University, Ames, Iowa 50011 United States

[¶]IKERBASQUE, Basque Foundation for Science, E-48011 Bilbao, Spain

S Supporting Information

ABSTRACT: We show that the chemical inhomogeneity in ternary three-dimensional topological insulators preserves the topological spin texture of their surface states against a net surface magnetization. The spin texture is that of a Dirac cone with helical spin structure in the reciprocal space, which gives rise to spin-polarized and dissipation-less charge currents. Thanks to the nontrivial topology of the bulk electronic structure, this spin texture is robust against most types of surface defects. However, magnetic perturbations break the time-reversal symmetry, enabling magnetic scattering and loss of spin coherence of the charge carriers. This intrinsic incompatibility precludes the design of magnetoelectronic devices based on the coupling between magnetic materials and topological surface states. We demonstrate that the magnetization coming from individual Co atoms deposited on the surface can disrupt the spin coherence of the carriers in the archetypal topological insulator Bi_2Te_3 , while in $\text{Bi}_2\text{Se}_2\text{Te}$ the spin texture remains unperturbed. This is concluded from the observation of elastic backscattering events in quasiparticle interference patterns obtained by scanning tunneling spectroscopy. The mechanism responsible for the protection is investigated by energy resolved spectroscopy and ab initio calculations, and it is ascribed to the distorted adsorption geometry of localized magnetic moments due to Se–Te disorder, which suppresses the Co hybridization with the surface states.

KEYWORDS: 3D topological insulators, magnetic atoms, chemical disorder, scanning tunneling microscopy, quasiparticle-interference pattern



The topological insulators (TI) $\text{Bi}_2(\text{Se}_x\text{Te}_{1-x})_3$ have a metallic surface state with a Dirac dispersion relation within the bulk band gap.^{1–3} It is called a topological surface state (TSS) because it arises from the combination of a topologically nontrivial electronic structure of the bulk and strong spin–orbit coupling.^{2,4,5} As a consequence, the TSS exhibits a helical spin structure due to spin–momentum locking.^{6–8} Thus, the probability of large scattering vectors (q) is dramatically suppressed^{9,10} since the initial state has null or negligible projection onto the final one in spin space. In particular, backscattering is quantum mechanically prohibited.^{6,9} This provides coherent spin currents in response to an electric field.

Given the size of the bulk bandgap of about 0.3 eV in $\text{Bi}_2(\text{Se}_x\text{Te}_{1-x})_3$, the TSS can be exploited even at room

temperature offering high electron mobility,¹¹ dissipation-less spin torque,¹² topological magnetoelectric coupling,¹³ or tunneling magnetoresistance.¹⁴ Another crucial advantage of TIs is that the functionalities of the surface are protected against any perturbation that preserves time reversal symmetry (TRS), such as contamination,¹⁵ structural defects,^{10,16} or phonon scattering.¹⁷ This is because the Dirac cone nature of the TSS is imposed by the nontrivial topology of the bulk.¹ However, to implement spintronic applications, materials with magnetic order have to be interfaced with the surface, breaking consequently TRS.^{18,19} Without TRS, the TSS becomes

Received: January 23, 2017

Revised: June 7, 2017

Published: June 13, 2017



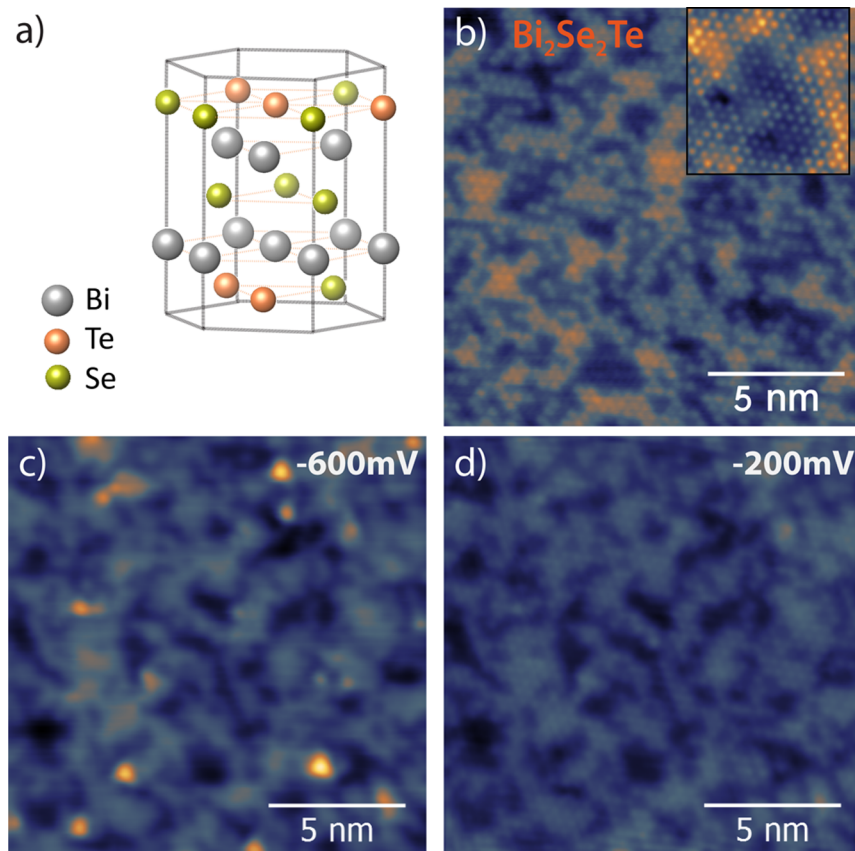


Figure 1. Constant current topography images of the pristine and Co-doped BST surface. (a) Layered unit cell structure of $\text{Bi}_2\text{Se}_2\text{Te}$ ($R\bar{3}m$ space group), showing the disordered occupation of Se/Te atoms in outer quintuple layers. (b) Atomically resolved STM image ($V_{\text{bias}} = -20$ mV, $I_{\text{set}} = 100$ pA). Bright and dark regions correspond to the electronic inhomogeneity of the same atomic layer, as can be appreciated in the inset (Z contrast 70 pm). (c,d) Topography images of the Co-doped surface of $\text{Bi}_2\text{Se}_2\text{Te}$ crystal taken at $V_{\text{bias}} = -600$ and -200 mV, respectively.

gapped^{19,20} and backscattering events are allowed since incoming electrons can exchange spin with the magnetic moment, turning the metallic states of the surface into trivial ones.²¹ In order to overcome this apparent contradiction, it is natural to explore interaction mechanisms between TSS and individual magnetic moments that preserve the TRS of the TI. TRS breaking can be probed by angle-resolved photoemission spectroscopy (ARPES), seeking the associated gap opening at the Dirac point.^{22,23} However, in ARPES experiments, the instrumental energy resolution and the Dirac node impurity band brought about by magnetic dopants (crossing the Dirac point)²⁰ hinder the gap opening caused by dispersed single magnetic atoms. On the other hand, quasiparticle interference (QPI) patterns obtained by scanning tunneling microscopy (STM) have proven to be extremely sensitive to minute amounts of scatterers.^{18,24} This technique pays attention to the emergence of q vectors associated with backscattering. Differential conductance (dI/dV) maps portray an image of the local density of states (LDoS) at energy $\epsilon = eV_{\text{bias}}$. Constructive interference among scattered surface electrons produce LDoS oscillations in real space from which the scattering intensity in q space can be mapped out by means of the fast Fourier transform (FFT) of the conductance image. In this Letter, we compare the impact of around 1% of ML of Co in the QPI patterns of $\text{Bi}_2(\text{Se}_{1-\delta}\text{Te}_{1+\delta})_3$ TIs with $\delta = 0$ and $\delta = 2/3$ (BST). We find that TRS is preserved in the ternary compound with $\delta = 2/3$, while in the binary compound with $\delta = 0$ TRS is destroyed.

Sample preparation, structural characterization, and conditioning of the (111) surface (in rhombohedral indexing) are described in the [Supporting Information](#). Cosublimation is performed by e-beam heating of high purity rods and keeping the sample below 5 K to avoid atom clustering. We fix the evaporation conditions to achieve a stable rate of 0.018 ± 0.002 ML/min, guaranteeing in this way a coverage regime with only single atoms on the surface (exemplified in [Supporting Information](#) Figure S1c). We define one monolayer (ML) coverage as one Co atom per surface unit cell. Scanning tunneling microscopy and spectroscopy have been performed in a low-temperature Specs JT-STM²⁵ with sample bias convention, base temperature of 4.3 K, and at a pressure better than 2×10^{-10} mbar. Further details on spectroscopy methods are given in the [Supporting Information](#).

Sessi et al.¹⁸ showed that doping Bi_2Te_3 with Mn atoms at the level of 1% of a ML is enough to induce backscattering spots in QPI patterns and therefore break TRS. For this to occur, the magnetic perturbation must have a finite stationary magnetization component perpendicular to the electron's wave vector.^{18,26,27} Note that a strong magnetic anisotropy with in-plane easy axis could mask a potential TRS breaking.^{28,29} In order to ensure a sizable out-of-plane Co magnetic moment, we perform our experiments under a 3 T field normal to the sample surface provided by a superconducting split coil. We have confirmed that this field strength is not enough to produce Landau quantization of the Dirac electrons, as expected for TSSs with scattering centers deposited on the surface.³⁰ In

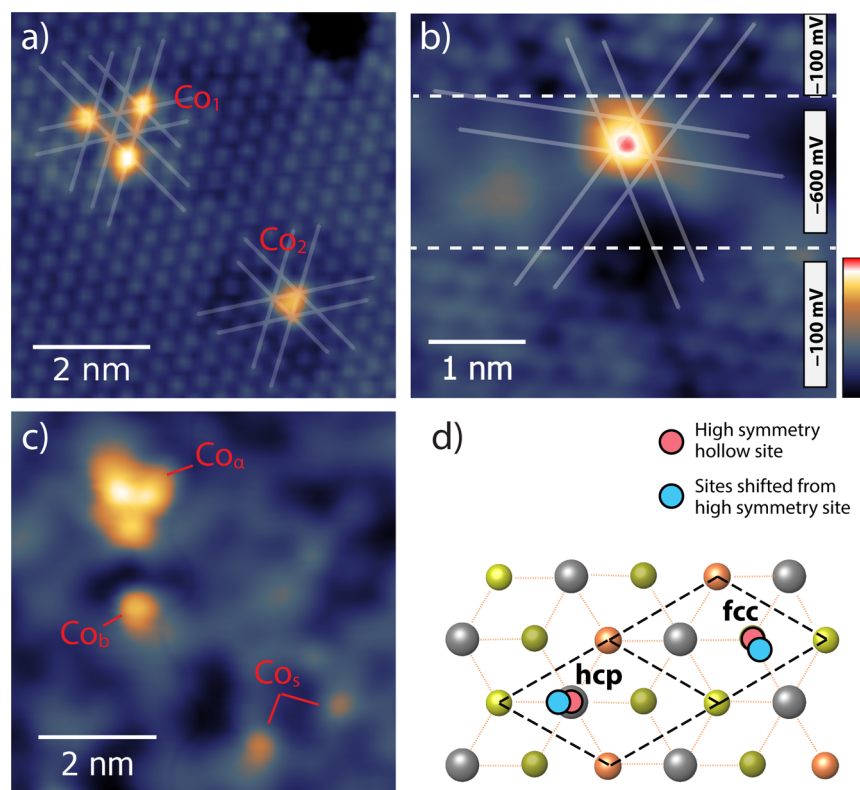


Figure 2. (a) Zoom in of the different apparent shapes of the Co atoms on Bi_2Te_3 ($V_{\text{bias}} = 450$ mV), Co atoms are found at two different high-symmetry adsorption (hcp and fcc) sites providing two Co apparent shapes. (b) In BST, to avoid that the tip sweeps away the adatoms due to the lack of Co states at low bias, different regulation set points are used to resolve the atom position and the surface structure. To do this, the topography is scanned at $V_{\text{bias}} = -100$ mV, -600 mV (over the atom) and again -100 mV during the same image. White lines are along closed packed directions of the crystal structure. Co atom site is shifted from the high symmetry hollow site. (c) Apparent shapes of Co atoms on BST ($V_{\text{bias}} = -600$ mV), we classified them into three categories called Co_a , Co_b , and Co_s . (d) Sketch of the $\text{Bi}_2\text{Se}_2\text{Te}(111)$ plane showing four of the 16 possible adsorption sites of Co atoms on this crystal. Red and blue circles represent the high-symmetry and shifted Co adsorption sites (for clarity, their shift is twice the theoretically calculated value).

particular, dI/dV spectra of the surface at 0 and 3 T fully overlap.

The crystal structure of $\text{Bi}_2(\text{Se}_{1-\delta}\text{Te}_{1+\delta})_3$ consists of stacks of quintuple layers, each formed by five atomic layers, along the [111] direction (see Figure 1a). The interaction between quintuple layers is weaker (van der Waals) than between the layers inside. Thus, these crystals are naturally cleaved along these outer layers (hexagonal faces in Figure 1a). For Bi_2Te_3 , the cleaved surface is Te-terminated as evidenced by the homogeneous atomically resolved STM topography (Supporting Information Figure S1). In contrast, BST topography presents an inhomogeneous surface segregated in regions of a few nanometers in size, as shown in Figure 1b. This segregation is due to the Se–Te chemical disorder, and it does not modify the crystalline structure shown in the inset of Figure 1b: BST and Bi_2Te_3 have the same hexagonal surface unit cell with just different lattice parameter. Similar surface inhomogeneity was reported for other bismuth-based TIs,¹⁰ but it is not observed in the binary compounds.⁶ In line with neutron diffraction refinements,³¹ cross sectional images in scanning transmission electron microscopy reveal that the outer layers have a 50:50 Te/Se random occupation (Supporting Information Figure S2). This disordered surface will be a key ingredient in the protection of TRS after Co deposition.

Individual Co atoms were deposited on the BST surface. The topography of the doped surface taken at $V_{\text{bias}} = -600$ mV displays a variety in the atoms appearance (Figure 1c).

Strikingly, the topography image of the very same region taken at -200 mV shows the total absence of Co atoms (Figure 1d), anticipating that there are no available states to tunnel to the tip at this energy. This does not occur on the Te homogeneous surface of Bi_2Te_3 . Here, Co atoms are found at two different high-symmetry hollow sites, namely fcc and hcp,^{18,32} providing two Co apparent shapes (Figure 2a). In contrast, the inhomogeneous surface of BST can alter the preferred Co site according to its specific environment giving rise to multiple adsorption geometries. With a random Se or Te occupation, a hollow site can have eight different environments: two high symmetry sites with three Se or three Te neighbors, three asymmetric sites with two Se neighbors and one Te, and three asymmetric sites with one Se and two Te neighbors. Note that each hollow site can be either fcc or hcp, resulting in a doubled multiplicity. We performed a thorough analysis of the adsorption sites (30 atoms from atomically resolved STM images as in Figure 2b), out of which we identified seven inequivalent sites out of the eight possible ones (a detailed description is given in Supporting Information Table S1). Most of them ($76 \pm 3\%$) undergo a remarkable shift away of the high-symmetry hollow sites, as is the case in Figure 2b. This deviation is confirmed by density-functional theory (DFT) calculations, which were performed applying the projector augmented-wave³³ method as implemented in the VASP code.^{34–36} We obtain the relaxed structure of Co atoms on a Bi_2Se_3 stack with substitutional Te in the outermost layer (see

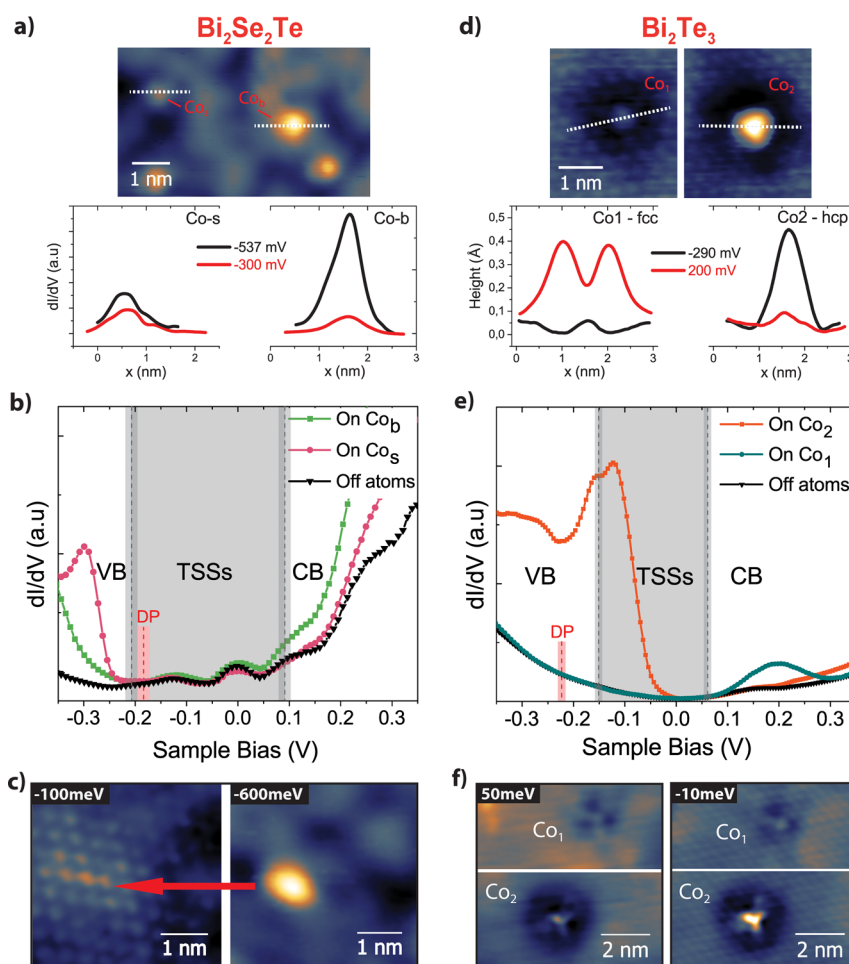


Figure 3. Lack of hybridization of Co states with Dirac TSSs on $\text{Bi}_2\text{Se}_2\text{Te}$. (a) Topography image ($V_{\text{bias}} = -600$ mV) showing Co_b and Co_s on BST (upper panel) and corresponding profiles along the dotted lines extracted from constant height dI/dV maps (bottom panel) at energies matching the resonances found in dI/dV spectra (see panel b). (b) dI/dV spectra obtained on the bare BST surface and on the two Co species shown in panel a. The three spectra were taken after opening the feedback over the surface at $V_{\text{bias}} = -200$ mV, $I_{\text{set}} = 50$ pA. The dashed red line marks the position of the Dirac point (DP) and the overlaid thick line gives the error stemming from linear fit of the dispersion relation (see Figure 5). Valence band (VB) and conduction band (CB) edges are indicated with black dashed lines, the thicker gray line giving the error coming from the uncertainty in the DP. The pale gray shaded area thus coincides with the bulk energy gap, a region populated exclusively by topological surface states (TSSs). (c) Constant current topography image of a Co_b (left) taken at $V_{\text{bias}} = -100$ mV displays just the BST lattice underneath the atom (red arrow points at the Co position), while the same atom is imaged at $V_{\text{bias}} = -600$ mV (right) as a prominent protrusion. (d) Topography images ($V_{\text{bias}} = -250$ mV) of the two types of high symmetry Co adsorption sites on Bi_2Te_3 and cross sectional profiles of their apparent shape along the dotted lines at different biases. (e) dI/dV spectra of Bi_2Te_3 and Co atoms shown in panel d, adsorbed on the two high symmetry hollow sites: fcc (Co_1) and hcp (Co_2). The setting bias chosen to open the feedback before acquiring the dI/dV spectra are 50 and 200 mV, respectively, where Co_1 and Co_2 display the minimum apparent height, which sets almost constant height conditions. (f) Constant current topographies of Co_1 and Co_2 atoms at 50 and -10 mV. Unlike on the BST crystal, Co atoms on Bi_2Te_3 possess large LDos inside the TSSs energy range, making them visible in topography at any V_{bias} within that region.

Supporting Information Table S2 and Note 2 for computational details). Based on the theoretical distortions, Figure 2d sketches possible adsorption geometries for the atom in Figure 2b. The typical apparent shapes of Co on BST at $V_{\text{bias}} = -600$ mV are shown in Figure 2c. From the statistical analysis of this kind of topographies without atomic resolution (near 1000 Co atoms included), we find that 99% of the Co atoms on BST can be classified into two categories: big round protrusions with height between 40 and 90 pm (hereafter Co_b) and smaller ones with heights between 20 and 30 pm (Co_s). Co_b and Co_s have almost the same abundance and are found in nonequivalent distorted adsorption sites, as detailed in Supporting Information Table S1, which suggests they might correspond to hollow sites surrounded by two Te (Co_b) or one Te (Co_s).

To get insight into the absence of tunneling current from the Co atoms at a certain V_{bias} , we performed dI/dV spectroscopy over Co_b and Co_s shown in Figure 3a. As seen in Figure 3b, the dI/dV spectra reveal an energy region where LDos on both species is identical to that of the surface. This energy region matches with great accuracy the bulk energy gap, where there are only TSSs. The absolute position of the band gap has been extracted from ARPES^{8,37} data of the same crystal shifted in energy to match our experimentally obtained dispersion relations. We note that these spectra were acquired in constant height conditions, so the tip distance to the BST surface is the same with or without Co atom underneath. The apparent height of single atoms on metals in STM ranges 50 to 100 pm. This entails an enormous change of conductance if one takes into account that the associated raise of tunneling probability is

199 exponential with barrier width. If the atom had just a small
 200 fraction of LDoS, it would be strongly enhanced by this
 201 constant height type of spectroscopy. Remarkably, we are even
 202 able to observe the surface lattice beneath the atom at $V_{\text{bias}} =$
 203 -100 mV, a value inside the TSSs energy region (Figure 3c).
 204 The invisibility of the atoms persists in the entire bulk band
 205 gap, as illustrated by Supplementary Figure S4a–o. Despite a
 206 certain variation in dI/dV spectra was observed for Co atoms
 207 outside the bulk bandgap region (Supporting Information
 208 Figure S5), likely related to the multiple adsorption sites, the
 209 overlap of spectra over atoms and over the surface within the
 210 bulk band gap is a reproducible feature. Consequently, the total
 211 absence of Co LDoS inside the TSSs energy range is a strong
 212 evidence for the lack of hybridization of Co states and the TSSs
 213 in BST.

214 Co_b atoms exhibit an atomic resonance far below the energy
 215 range of the Dirac cone, at around -550 mV (see
 216 Supplementary Figure S5), which is responsible for their larger
 217 apparent height in topography at -600 mV (Figure 3a). The
 218 resonance found in Co_s slightly below the Dirac point at -300
 219 mV (Figure 3b) can be interpreted as a true atomic state, or
 220 alternatively as the fingerprint of a bound state owing to the
 221 confining electrostatic potential created by a point-like
 222 impurity.²⁰ In the latter case, the coupling mechanism is of
 223 purely electrostatic origin, which cannot induce magnetic
 224 coupling between the TSS and the Co moment. In addition,
 225 taking into account the spatial extent of this resonance of less
 226 than 1 nm observed in the red profiles of Figure 3a, the average
 227 interatomic distance of ca. 6 nm in our sample impedes the
 228 formation of a delocalized bound state band. In the case that
 229 the Co_s resonance stems from an atomic orbital, its spectral
 230 weight in the region of TSS is given by the small tail of the
 231 onset starting right at the Dirac point, where the TSS density of
 232 states is minimal. Altogether, the coupling of Co_s atoms to the
 233 TSS can be considered marginal.

234 In contrast to BST, Figure 3e shows strong LDoS resonances
 235 within the TSSs region of Co atoms adsorbed on Bi_2Te_3 , in
 236 particular the ones shown in Figure 3d. On this surface, the
 237 atoms are visible in constant current topography images inside
 238 the entire bulk band gap region (Figure 3f), and certainly at the
 239 energy position corresponding to the resonances found at the
 240 two high symmetry Co adsorption sites (Figure 3d). Therefore,
 241 in this case there are Co states and TSS coexisting at the same
 242 energy.

243 Now we turn our attention to QPI patterns of the pristine
 244 BST and Bi_2Te_3 surfaces. The spin-texture of TSSs prohibits
 245 backscattering.^{9,10} However, due to the hexagonal warping of
 246 the Dirac cone at high energies, some scattering channels that
 247 are fully compatible with TRS open up.^{38,39} In the warped
 248 region of TSSs, electrons propagating along the ΓK direction of
 249 the surface Brillouin zone acquire an out-of-plane spin
 250 component, which is of the same sign in alternate K points.
 251 This gives rise to q vectors parallel to the ΓM direction (see
 252 sketch in Figure 5c), that are detected in the FFT dI/dV maps
 253 of undoped surfaces as energy dispersing bright spots along the
 254 ΓM direction with 6-fold symmetry, Figure 4. In Figure 5a,b,
 255 we show the dependence of $q_{\Gamma\text{M}}$ on energy (black symbols),
 256 where the expected linear dispersion for Dirac Fermions in
 257 both Bi_2Te_3 and BST is observed. For energies near the Dirac
 258 point (DP), the hexagonal warping is so weak that scattering
 259 along ΓM extinguishes. The ΓM scattering allows us to obtain
 260 the DP by fitting the dispersion relation to a linear regression.
 261 In the case of the BST crystal, to accurately locate the DP we

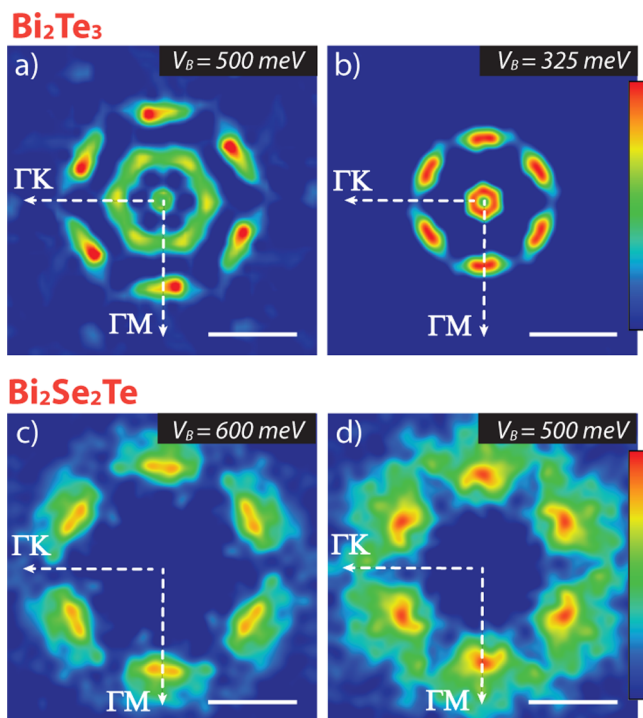


Figure 4. Quasiparticle interference scattering patterns on the bare $\text{Bi}_2\text{Se}_2\text{Te}$ and Bi_2Te_3 surfaces. FFTs obtained from the dI/dV maps of the Bi_2Te_3 (a,b) and $\text{Bi}_2\text{Se}_2\text{Te}$ (c,d) bare surfaces at the warped energy region of the Dirac cone. Raw FT were 6-fold symmetrized and normalized to the respective average dI/dV signal. Both compounds present scattering vectors along the ΓM direction, $q_{\Gamma\text{M}}$. The dependence of $q_{\Gamma\text{M}}$ on V_{bias} follows the expected linear dispersion for Dirac Fermions in both Bi_2Te_3 and BST, as shown in Figure 5. White scale bars correspond to 3 nm^{-1} . Dashed lines represent ΓK and ΓM directions.

262 took into account a slight change in the slope of the Dirac cone
 263 near the DP⁸ (thick lines in Figure 5b). After Co doping of
 264 BST and Bi_2Te_3 surfaces, just by looking at the dispersion of
 265 ΓM scattering, we find that the entire Dirac cone has shifted
 266 approximately 100 meV to lower energies in both Bi_2Te_3 and
 267 BST crystals, confirming the electron donor character of Co
 268 atoms.^{23,28,39} This is in agreement with the overall shift toward
 269 lower energies experienced by the dI/dV spectra of the bare
 270 surface after doping. However, more remarkably, Figure 5c
 271 shows that, while Co doping induces strong scattering spots
 272 along ΓK in Bi_2Te_3 , this contribution is totally absent in BST.

273 The comparison of Co mediated scattering between both
 274 surfaces in the ΓK directions is our central result. Figure 5c
 275 displays the FFT dI/dV maps at energies for which the q range
 276 lies between 1 and 2.5 nm^{-1} , comparing the same q values for
 277 both samples in order to sample the reciprocal space with the
 278 same resolution. As mapping energy ($\epsilon = eV_{\text{bias}}$) approaches the
 279 Dirac point, new scattering channels along ΓK in Bi_2Te_3 are
 280 progressively reinforced; while the scattering ascribed exclu-
 281 sively to hexagonal warping ($q_{\Gamma\text{M}}$) weakens due to the
 282 depopulation of the warped regions.^{3,40} The dispersion relation
 283 of $q_{\Gamma\text{K}}$ follows the expected behavior for backscattering taking
 284 into account the scattering geometry of the constant energy
 285 contours (see middle row in Figure 5c). This means that $q_{\Gamma\text{K}}(\epsilon)$
 286 should coincide with the line $q_{\Gamma\text{M}}(\epsilon)/\cos(30^\circ)$, both lines
 287 intersecting the ordinate axis at the Dirac point, as is the case of
 288 the scattering patterns along ΓK from Co/ Bi_2Te_3 (Figure 5a).
 289 Then, we can unambiguously conclude that Co doping opens

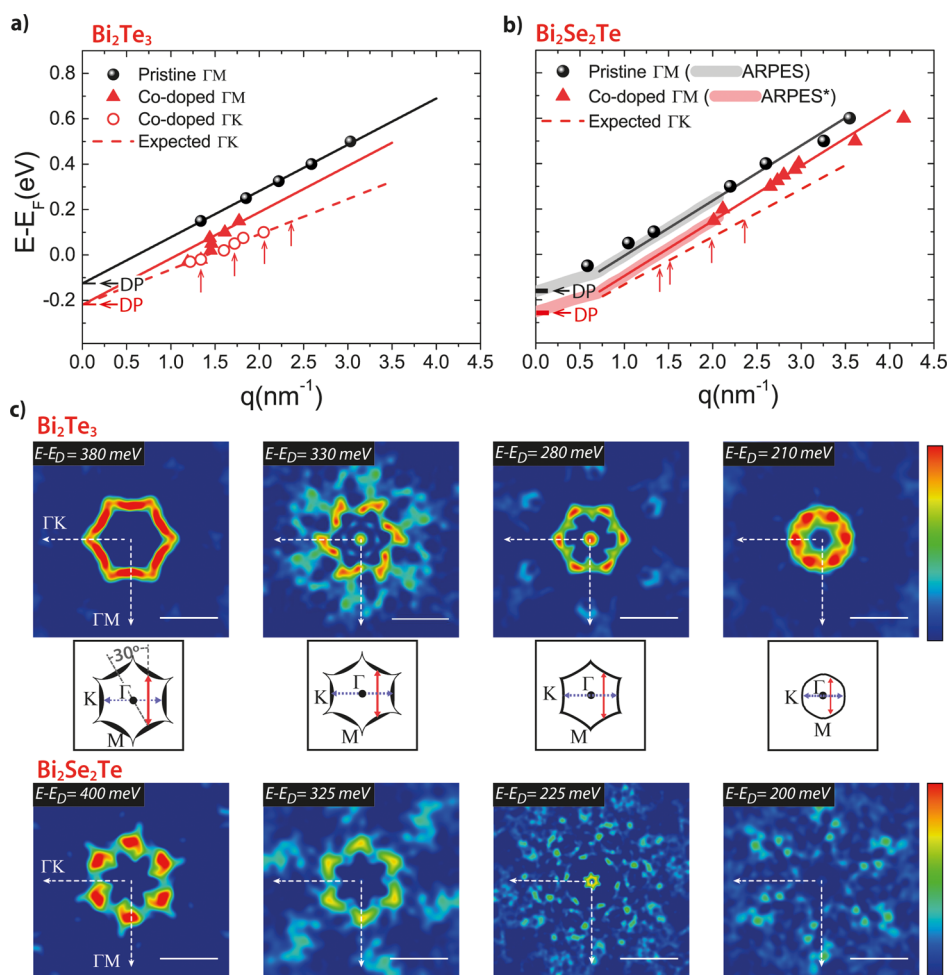


Figure 5. Quasiparticle interference scattering patterns in Co-doped Bi₂Se₂Te and Bi₂Te₃ under a 3 T magnetic field normal to the surface. (a,b) Energy dispersion in Bi₂Te₃ and BST, respectively, inferred from the analysis of FFTs. The Dirac point of the bare surface (corresponding FFTs shown in Figure 4) is obtained by the linear fitting of the data along ΓM (black dots) yielding $E_D = -131 \pm 14$ meV in Bi₂Te₃ and $E_D = -154 \pm 11$ meV in BST. One percent Co-doping induces a shift toward lower energies of about 100 meV (red triangles). Bi₂Te₃ FFTs spots along ΓK show linear dispersion pointing also to the Dirac point, at -220 ± 4 meV, ascribed to backscattering processes (red empty dots). Red dashed lines denote the expected dispersion for backscattering (if allowed) vectors (ΓK) derived from the $q_{\Gamma M}$ dispersion (see text). (c) Fast Fourier transform of the dI/dV images of Co-doped Bi₂Te₃ (0.012 ML Co, upper row) and BST (0.015 ML Co, bottom row) in an out-of-plane magnetic field of 3 T. The energy range eV_{bias} is chosen so that the scattering vectors have similar value (vertical arrows in panels a,b), resulting in the same resolution in reciprocal space. White scale bars correspond to 3 nm⁻¹. Middle row: Sketch of constant energy contour of the warped surface states in the reciprocal space, where the scattering vectors $q_{\Gamma M}$ and $q_{\Gamma K}$ are indicated as red and gray arrows.

backscattering channels at an applied field of 3 T and therefore breaks TRS.

The scenario in BST is very different (Figure 5c, bottom row). QPI patterns along ΓM direction persist after Co doping, but no intensity was detected along the ΓK direction at any V_{bias} around Fermi level. A quenching of the Co magnetic moment upon adsorption in BST is ruled out from the robust magnetic moment of Co, ranging 1.4 to 2.0 μ_B , obtained in DFT calculations for the disordered surface (Supporting Information Table S2). To discard a possible magnetic or structural coupling among Co sites in BST, we have confirmed that the ground state magnetic moment is robust against a coverage decrease from 0.25 to 0.11 ML. According to the calculations, the overall easy axis for the magnetic moment is out-of-plane. Only 25% of Co sites relax to a ground state with larger in-plane magnetization component. In those cases, the weak magneto-crystalline anisotropy can be overcome by the 3 T out-of-plane field (Supporting Information Note 2), as was found for the magnetic dichroism of 0.01 ML Co on Bi₂Se₃.⁴¹

To conclude, in spite of the introduction of TRS breaking perturbations of the same strength as in Bi₂Te₃, backscattering remains prohibited in BST, and therefore, the TSSs is robust against the perturbation. From the analysis of backscattering patterns, we find that TRS is preserved in the Se–Te mixed surface termination of BST under the same coverage and experimental conditions for which TRS is destroyed in the Te-terminated surface of Bi₂Te₃. Furthermore, dI/dV spectroscopy reveals the absence of Co states within the bulk band gap of BST, the energy region where only TSS exist. This evidences that the modified adsorption geometry in the disordered surface precludes Co magnetic states from hybridizing with the TSS, preserving in this way TRS. This principle can be expected to apply in many other ternary TIs, enabling the design of functional interfaces based on magnetic probes in close contact to topological surface states.

ASSOCIATED CONTENT

Supporting Information

The Supporting Information is available free of charge on the ACS Publications website at DOI: 10.1021/acs.nanolett.7b00311.

Details on sample preparation and experimental set up, together with figures and tables with topography images of the Co adsorption geometry, HRTEM cross sectional views of the crystals, detailed spectroscopy data, and computational parameters (PDF)

AUTHOR INFORMATION

Corresponding Author

*E-mail: serrate@unizar.es (D.S.).

ORCID

Bernhard Kretz: 0000-0002-6728-1025

Myriam H. Aguirre: 0000-0002-1296-4793

Luis Morellón: 0000-0003-3724-508X

Arán Garcia-Lekue: 0000-0001-5556-0898

David Serrate: 0000-0002-3260-9641

Present Addresses

(M.C.M.-V.) Department of Quantum Nanoscience, Delft University of Technology, Lorentzweg 1, 2628 CJ Delft, The Netherlands.

(M.M.-L.) Institute of Physics, Academy of Sciences of the Czech Republic, Prague, Czech Republic. Regional Centre of Advanced Technologies and Materials, Faculty of Science, Department of Physical Chemistry, Palacky University, Olomouc, Czech Republic.

Notes

The authors declare no competing financial interest.

ACKNOWLEDGMENTS

We acknowledge the use of SAI-Universidad de Zaragoza. T.M.R. and T.A.L. acknowledge support by the U.S. Department of Energy (DOE), Office of Science, Basic Energy Sciences, Materials Science and Engineering Division. Ames Laboratory is operated for the U.S. DOE by Iowa State University under contract DE-AC02-07CH11358. Financial support was provided from Spanish MINECO (MAT2013-46593-C6-3-P, MAT2013-46593-C6-2-P and MAT2014-51982-C-R), European Commission (FP-7-PEOPLE-304043), and Gobierno de Aragón (E26). B.K. and A.G.L. were also funded by the Basque Departamento de Educación (IT-756-13).

ABBREVIATIONS

TI, topological insulator; TSS, topological surface state; TRS, time reversal symmetry; ARPES, angle resolved photoemission spectroscopy; QPI, quasiparticle interference; STM, scanning tunneling microscopy; LDoS, local density of states; FFT, fast Fourier transform; BST, Bi₂Se₃Te; ML, monolayer; DFT, density functional theory; DP, Dirac point; EPMA, automated electron microprobe; HAADF, high angular annular dark field; GGA, generalized gradient approximation; PBE, Perdew–Burke–Enzerhof; VB, valence band; CB, conduction band

REFERENCES

(1) Zhang, H.; Liu, C.-X.; Qi, X.-L.; Dai, X.; Fang, Z.; Zhang, S.-C. *Nat. Phys.* **2009**, *5*, 438–442.

(2) Xia, Y.; Qian, D.; Hsieh, D.; Wray, L.; Pal, A.; Lin, H.; Bansil, A.; Grauer, D.; Hor, Y. S.; Cava, R. J.; Hasan, M. Z. *Nat. Phys.* **2009**, *5*, 398–402.

(3) Chen, Y. L.; Analytis, J. G.; Chu, J.-H.; Liu, Z. K.; Mo, S.-K.; Qi, X. L.; Zhang, H. J.; Lu, D. H.; Dai, X.; Fang, Z.; Zhang, S. C.; Fisher, I. R.; Hussain, Z.; Shen, Z.-X. *Science* **2009**, *325*, 178–181.

(4) Kane, C. L.; Mele, E. J. *Phys. Rev. Lett.* **2005**, *95*, 146802.

(5) Moore, J. E. *Nature* **2010**, *464*, 194–198.

(6) Zhang, T.; Cheng, P.; Chen, X.; Jia, J.-F.; Ma, X.; He, K.; Wang, L.; Zhang, H.; Dai, X.; Fang, Z.; Xie, X.; Xue, Q.-K. *Phys. Rev. Lett.* **2009**, *103*, 266803.

(7) Hsieh, D.; Xia, Y.; Qian, D.; Wray, L.; Dil, J. H.; Meier, F.; Osterwalder, J.; Patthey, L.; Checkelsky, J. G.; Ong, N. P.; Fedorov, A. V.; Lin, H.; Bansil, A.; Grauer, D.; Hor, Y. S.; Cava, R. J.; Hasan, M. Z. *Nature* **2009**, *460*, 1101–1105.

(8) Miyamoto, K.; Kimura, A.; Okuda, T.; Miyahara, H.; Kuroda, K.; Namatame, H.; Taniguchi, M.; Ereemeev, S. V.; Menshchikova, T. V.; Chulkov, E. V.; Kokh, K. A.; Tereshchenko, O. E. *Phys. Rev. Lett.* **2012**, *109*, 166802.

(9) Roushan, P.; Seo, J.; Parker, C. V.; Hor, Y. S.; Hsieh, D.; Qian, D.; Richardella, A.; Hasan, M. Z.; Cava, R. J.; Yazdani, A. *Nature* **2009**, *460*, 1106–1109.

(10) Kim, S.; Yoshizawa, S.; Ishida, Y.; Eto, K.; Segawa, K.; Ando, Y.; Shin, S.; Komori, F. *Phys. Rev. Lett.* **2014**, *112*, 136802.

(11) Taskin, A. A.; Sasaki, S.; Segawa, K.; Ando, Y. *Phys. Rev. Lett.* **2012**, *109*, 66803.

(12) Garate, I.; Franz, M. *Phys. Rev. Lett.* **2010**, *104*, 146802.

(13) Qi, X.-L.; Hughes, T. L.; Zhang, S.-C. *Phys. Rev. B: Condens. Matter Mater. Phys.* **2008**, *78*, 195424.

(14) Dankert, A.; Geurs, J.; Kamalakar, M. V.; Charpentier, S.; Dash, S. P. *Nano Lett.* **2015**, *15*, 7976–7981.

(15) Yashina, L. V.; Sánchez-Barriga, J.; Scholz, M. R.; Volykhov, A. A.; Sirotina, A. P.; Neudachina, V. S.; Tamm, M. E.; Varykhalov, A.; Marchenko, D.; Springholz, G.; Bauer, G.; Knop-Gericke, A.; Rader, O. *ACS Nano* **2013**, *7*, 5181–5191.

(16) Pielmeier, F.; Landolt, G.; Slomski, B.; Muff, S.; Berwanger, J.; Eich, A.; Khajetoorians, A. A.; Wiebe, J.; Aliev, Z. S.; Babanly, M. B.; Wiesendanger, R.; Osterwalder, J.; Chulkov, E. V.; Giessibl, F. J.; Dil, J. *H. New J. Phys.* **2015**, *17*, 23067.

(17) Pan, Z.-H.; Fedorov, A. V.; Gardner, D.; Lee, Y. S.; Chu, S.; Valla, T. *Phys. Rev. Lett.* **2012**, *108*, 187001.

(18) Sessi, P.; Reis, F.; Bathon, T.; Kokh, K. A.; Tereshchenko, O. E.; Bode, M. *Nat. Commun.* **2014**, *5*, 5349.

(19) Chen, Y. L.; Chu, J.-H.; Analytis, J. G.; Liu, Z. K.; Igarashi, K.; Kuo, H.-H.; Qi, X. L.; Mo, S. K.; Moore, R. G.; Lu, D. H.; Hashimoto, M.; Sasagawa, T.; Zhang, S. C.; Fisher, I. R.; Hussain, Z.; Shen, Z. X. *Science (Washington, DC, U. S.)* **2010**, *329*, 659–662.

(20) Sessi, P.; Biswas, R. R.; Bathon, T.; Storz, O.; Wilfert, S.; Barla, A.; Kokh, K. A.; Tereshchenko, O. E.; Fauth, K.; Bode, M.; Balatsky, A. V. *Nat. Commun.* **2016**, *7*, 12027.

(21) Xu, S.-Y.; Neupane, M.; Liu, C.; Zhang, D.; Richardella, A.; Andrew Wray, L.; Alidoust, N.; Leandersson, M.; Balasubramanian, T.; Sánchez-Barriga, J.; Rader, O.; Landolt, G.; Slomski, B.; Hugo Dil, J.; Osterwalder, J.; Chang, T.-R.; Jeng, H.-T.; Lin, H.; Bansil, A.; Samarth, N.; Zahid Hasan, M. *Nat. Phys.* **2012**, *8*, 616–622.

(22) Schlenk, T.; Bianchi, M.; Koleini, M.; Eich, A.; Pietzsch, O.; Wehling, T. O.; Frauenheim, T.; Balatsky, A.; Mi, J.-L.; Iversen, B. B.; Wiebe, J.; Khajetoorians, A. A.; Hofmann, P.; Wiesendanger, R. *Phys. Rev. Lett.* **2013**, *110*, 126804.

(23) Scholz, M. R.; Sánchez-Barriga, J.; Marchenko, D.; Varykhalov, A.; Volykhov, A.; Yashina, L. V.; Rader, O. *Phys. Rev. Lett.* **2012**, *108*, 1–5.

(24) Pascual, J. I.; Bihlmayer, G.; Koroteev, Y. M.; Rust, H.-P.; Ceballos, G.; Hansmann, M.; Horn, K.; Chulkov, E. V.; Blügel, S.; Echenique, P. M.; Hofmann, P. *Phys. Rev. Lett.* **2004**, *93*, 196802.

(25) Zhang, L.; Miyamachi, T.; Tomanić, T.; Dehm, R.; Wulfhekel, W. *Rev. Sci. Instrum.* **2011**, *82*, 103702.

(26) Narayan, A.; Rungger, I.; Sanvito, S. *New J. Phys.* **2015**, *17*, 33021.

- 450 (27) Liu, Q.; Liu, C.-X.; Xu, C.; Qi, X.-L.; Zhang, S.-C. *Phys. Rev. Lett.*
451 **2009**, *102*, 156603.
- 452 (28) Ye, M.; Eremeev, S. V.; Kuroda, K.; Krasovskii, E. E.; Chulkov,
453 E. V.; Takeda, Y.; Saitoh, Y.; Okamoto, K.; Zhu, S. Y.; Miyamoto, K.;
454 Arita, M.; Nakatake, M.; Okuda, T.; Ueda, Y.; Shimada, K.; Namatame,
455 H.; Taniguchi, M.; Kimura, A. *Phys. Rev. B: Condens. Matter Mater.*
456 *Phys.* **2012**, *85*, 205317.
- 457 (29) Honolka, J.; Khajetoorians, A. A.; Sessi, V.; Wehling, T. O.;
458 Stepanow, S.; Mi, J.-L.; Iversen, B. B.; Schlenk, T.; Wiebe, J.; Brookes,
459 N. B.; Lichtenstein, A. I.; Hofmann, P.; Kern, K.; Wiesendanger, R.
460 *Phys. Rev. Lett.* **2012**, *108*, 256811.
- 461 (30) Cheng, P.; Zhang, T.; He, K.; Chen, X.; Ma, X.; Xue, Q. *Phys. E*
462 **2012**, *44*, 912–916.
- 463 (31) Park, K.; Nomura, Y.; Arita, R.; Llobet, A.; Louca, D. *Phys. Rev.*
464 *B: Condens. Matter Mater. Phys.* **2013**, *88*, 224108.
- 465 (32) Eelbo, T.; Waśniowska, M.; Sikora, M.; Dobrzański, M.;
466 Kozłowski, A.; Pulkin, A.; Autès, G.; Miotkowski, I.; Yazyev, O. V.;
467 Wiesendanger, R. *Phys. Rev. B: Condens. Matter Mater. Phys.* **2014**, *89*,
468 104424.
- 469 (33) Blöchl, P. E. *Phys. Rev. B: Condens. Matter Mater. Phys.* **1994**, *50*,
470 17953–17979.
- 471 (34) Kresse, G.; Hafner, J. *Phys. Rev. B: Condens. Matter Mater. Phys.*
472 **1993**, *47*, 558–561.
- 473 (35) Kresse, G.; Furthmüller, J. *Comput. Mater. Sci.* **1996**, *6*, 15–50.
- 474 (36) Kresse, G.; Furthmüller, J. *Phys. Rev. B: Condens. Matter Mater.*
475 *Phys.* **1996**, *54*, 11169–11186.
- 476 (37) Bao, L.; He, L.; Meyer, N.; Kou, X.; Zhang, P.; Chen, Z.-G.;
477 Fedorov, A. V.; Zou, J.; Riedemann, T. M.; Lograsso, T. a; Wang, K.
478 L.; Tuttle, G.; Xiu, F. *Sci. Rep.* **2012**, *2*, 726.
- 479 (38) Jung, W.; Kim, Y.; Kim, B.; Koh, Y.; Kim, C.; Matsunami, M.;
480 Kimura, S.; Arita, M.; Shimada, K.; Han, J. H.; Kim, J.; Cho, B.; Kim,
481 C. *Phys. Rev. B: Condens. Matter Mater. Phys.* **2011**, *84*, 245435.
- 482 (39) Alpichshev, Z.; Analytis, J. G.; Chu, J.-H.; Fisher, I. R.; Chen, Y.
483 L.; Shen, Z. X.; Fang, A.; Kapitulnik, A. *Phys. Rev. Lett.* **2010**, *104*,
484 16401.
- 485 (40) Fu, L. *Phys. Rev. Lett.* **2009**, *103*, 1–4.
- 486 (41) Waśniowska, M.; Sikora, M.; Dobrzański, M.; Eelbo, T.; Soares,
487 M. M.; Rams, M.; Miotkowski, I.; Wiesendanger, R.; Berndt, R.; Kąkol,
488 Z.; Kozłowski, A. *Phys. Rev. B: Condens. Matter Mater. Phys.* **2015**, *92*,
489 115412.